



# Visible-light-responsive graphene-functionalized Bi-bridge Z-scheme black BiOCl/Bi<sub>2</sub>O<sub>3</sub> heterojunction with oxygen vacancy and multiple charge transfer channels for efficient photocatalytic degradation of 2-nitrophenol and industrial wastewater treatment

Fang Deng<sup>a</sup>, Qian Zhang<sup>a</sup>, Lixia Yang<sup>a</sup>, Xubiao Luo<sup>a</sup>, Aijie Wang<sup>b</sup>, Shenglian Luo<sup>a,\*</sup>, Dionysios D. Dionysiou<sup>c</sup>

<sup>a</sup> Key Laboratory of Jiangxi Province for Persistent Pollutants Control and Resources Recycle, Nanchang Hangkong University, Nanchang 330063, PR China

<sup>b</sup> Research Center for Eco-Environmental Sciences, Chinese Academy of Sciences, Beijing 100085, PR China

<sup>c</sup> Department of Chemical and Environmental Engineering (DCEE), University of Cincinnati, Cincinnati, OH 45221-0012, USA



## ARTICLE INFO

**Keywords:**  
black BiOCl-Bi-Bi<sub>2</sub>O<sub>3</sub>/rGO heterojunction  
Oxygen vacancy  
Multiple charge transfer channels  
Photocatalytic activity  
Industrial wastewater treatment

## ABSTRACT

Although Bi-based compounds are effective photocatalysts for degrading organic pollutants under visible-light irradiation, their visible-light photocatalytic activities are still low and far from practical application. In this study, novel graphene-functionalized Bi-bridge Z-scheme black BiOCl/Bi<sub>2</sub>O<sub>3</sub> (black BiOCl-Bi-Bi<sub>2</sub>O<sub>3</sub>/rGO) heterojunctions with oxygen vacancies were prepared via in situ Fe reduction of BiOCl/graphene oxide nanoplates. In comparison with BiOCl/graphene oxide nanoplates, the black BiOCl-Bi-Bi<sub>2</sub>O<sub>3</sub>/rGO heterojunctions have stronger visible-light absorption, and exhibit more efficient charge separation and higher visible-light photocatalytic activity in degrading 2-nitrophenol (2NP). The black BiOCl-Bi-Bi<sub>2</sub>O<sub>3</sub>/rGO<sub>0.4</sub> shows the highest visible-light photocatalytic activity with almost complete degradation of 2NP, which is attributed to proper bandgap match between black BiOCl and Bi<sub>2</sub>O<sub>3</sub>, multiple charge transfer channels via Bi-bridge and rGO, and efficient charge separation. Of special importance, black BiOCl-Bi-Bi<sub>2</sub>O<sub>3</sub>/rGO heterojunction can effectively treat real industrial wastewater with 70.3% COD removal efficiency, and it shows superior long-term stability. Additionally, a possible photocatalytic mechanism of black BiOCl-Bi-Bi<sub>2</sub>O<sub>3</sub>/rGO heterojunctions based on multiple charge transfer channels was proposed.

## 1. Introduction

The discharge of industrial wastewater is the main cause of water pollution. Drinking contaminated water for a long time poses potential risks to human health, even can cause cancer, teratogenicity, and mutagenicity [1–3]. Thus, it is very urgent to develop some efficient techniques to treat real industrial wastewater for meeting the emission standards.

Semiconductor photocatalysis has been considered as an efficacious and sustainable technique for wastewater treatment [4–7]. The traditional photocatalysts (such as TiO<sub>2</sub> and ZnO) with wide band gap are active only in ultraviolet (UV) region, and the rapid recombination rate of the photogenerated electrons and holes leads to a low quantum efficiency, which limits their practical application in wastewater treatment [8–10]. With the aim of amending the drawbacks of traditional

photocatalysts, novel Bi-based semiconductor photocatalysts have been developed and widely studied. Among Bi-based photocatalysts, bismuth oxychloride (BiOCl) has attracted tremendous concern because of its unique optical and electrical properties, fascinating physicochemical properties, non-toxicity, high chemical and corrosion resistance, and higher UV-light photocatalytic activity than TiO<sub>2</sub> in degrading organic compounds [11,12]. Similarly to TiO<sub>2</sub>, BiOCl has large band gap of 3.4 eV, and is only activated with UV-light, leading to poor visible-light photocatalytic activity [13,14]. Therefore, some strategies have been proposed to improve the visible-light photocatalytic activity of BiOCl by band-gap engineering.

The formation of black BiOCl materials with oxygen vacancies has been considered to be an efficient strategy to decrease its band gap, enhance visible-light absorption and photocatalytic activity [15–17]. However, black BiOCl still suffers from the rapid recombination of

\* Corresponding author.

E-mail address: [sllou@hnu.edu.cn](mailto:sllou@hnu.edu.cn) (S. Luo).

photogenerated charge carriers, and its photocatalytic activity is still not satisfactory. Constructing heterojunction of black BiOCl with other suitable photocatalysts has been accepted as an effective and simple strategy to solve the above problems to a certain degree [18–20]. The matched band-gap structure between black BiOCl and Bi<sub>2</sub>O<sub>3</sub> is suitable for fabricating heterojunction photocatalysts, and found that the photocatalytic activity of black BiOCl/Bi<sub>2</sub>O<sub>3</sub> heterojunctions was higher than that of individual components [21]. Despite the improved charge separation and photocatalytic activity of common heterojunction photocatalysts, the redox ability of the semiconductor heterojunctions decreases in comparison with its single components, thus limiting practical application.

Recently, Z-scheme heterojunctions have attracted huge interest. Z-scheme heterojunctions not only facilitate the charge separation and transfer, but also maintain the redox ability of their components [22–24]. The charge transfer in Z-scheme photocatalysts is mainly via interface defects and Z-scheme bridges (metals, such as Au and Ag) [25]. Due to the excellent conductivity of metal, metal conductors (Ag, Au, Pt and Bi) are usually used as charge transfer channels between two semiconductors [26–28]. Because of the excellent properties of metallic Bi such as low cost, highly anisotropic Fermi surface, low carrier density, long carrier mean free path and small band gap, the Bi-bridge Z-scheme black BiOCl/Bi<sub>2</sub>O<sub>3</sub> heterojunctions are worth researching. However, the problems of heterojunction photocatalysts prepared by common chemical methods are lattice mismatch between two semiconductors and low proportion of structural elements with intimate interface. Due to the large surface area and superior electron mobility of graphene, functionalized graphene-based semiconductor photocatalysts could deal well with the above-mentioned issues.

In our study, we developed a novel graphene-functionalized Bi-bridge Z-scheme black BiOCl/Bi<sub>2</sub>O<sub>3</sub> heterojunction with oxygen vacancies (black BiOCl-Bi<sub>2</sub>O<sub>3</sub>/rGO) via *in situ* Fe reduction of BiOCl/graphene oxide nanoplates, which provides tight solid-solid contact interface and strong interaction among Bi, black BiOCl, Bi<sub>2</sub>O<sub>3</sub> and rGO, and is beneficial for charge separation and transfer. Proper bandgap matching between black BiOCl and Bi<sub>2</sub>O<sub>3</sub>, Bi-bridge and rGO charge transfer channels, and efficient charge separation play synergistic roles in the high photocatalytic performance of black BiOCl-Bi<sub>2</sub>O<sub>3</sub>/rGO heterojunction. Black BiOCl-Bi<sub>2</sub>O<sub>3</sub>/rGO heterojunction not only shows high photocatalytic degradation efficiency for 2-nitrophenol, but only can efficaciously treat real industrial wastewater with high COD removal efficiency. It is noteworthy that the black BiOCl-Bi<sub>2</sub>O<sub>3</sub>/rGO heterojunctions exhibit superior long-term photo-stability. Moreover, a possible photocatalytic mechanism of black BiOCl-Bi<sub>2</sub>O<sub>3</sub>/rGO heterojunctions based on multiple charge transfer channels was proposed to explain the underlying phenomena taking place in the process.

## 2. Experimental section

### 2.1. Chemicals

Potassium chloride (KCl, 98.5%) and reduced iron powder were purchased from Tianjin Fuchen Chemical Reagent Co., Ltd. Bismuth nitrate pentahydrate (Bi(NO<sub>3</sub>)<sub>3</sub>·5H<sub>2</sub>O, 99%), hydrochloric acid (36–38%), triethanolamine (TEOA) and isopropanol (IPA) were purchased from Shantou Xilong Chemical Co., Ltd. (Shantou, China). Ammonia solution (NH<sub>3</sub>·H<sub>2</sub>O, 25–28%) was provided by Nanchang Xinguang Fine Chemical Factory (Nanchang, China). 2-nitrophenol (2NP) and nitroblue tetrazolium chloride (NBT, 98%) were obtained from Shanghai Aladdin Biochemical Technology Co., Ltd (Shanghai, China). Aqueous dispersion of graphene oxide was acquired from Leader Nano Technology Co., Ltd. (Jining, China). The real industrial wastewater was selected from the wastewater discharge tank of Jiangxi Chemedir Biopharm-tech. Co., Ltd.

### 2.2. The preparation of BiOCl/GO

First, 0.02 mol of KCl was dissolved in 150 mL of GO solution, and then 0.02 mol of Bi(NO<sub>3</sub>)<sub>3</sub>·5H<sub>2</sub>O was fully dissolved in the above solution under magnetic stirring, and a certain amount of NH<sub>3</sub>·H<sub>2</sub>O solution was added to adjust the solution pH to 10, then the reaction mixture was magnetically stirred for 12 h at room temperature. The obtained gray-white precipitate was fully washed with deionized water until the eluent was neutral, and then it was dried at 60 °C for 12 h. According to GO mass (g) in the reaction system, BiOCl/GO samples were denoted as BiOCl/GO<sub>0.02</sub>, BiOCl/GO<sub>0.08</sub>, BiOCl/GO<sub>0.2</sub>, BiOCl/GO<sub>0.4</sub> and BiOCl/GO<sub>0.6</sub>.

For comparison purpose, pure BiOCl was similarly prepared in aqueous solution without GO as above.

### 2.3. The preparation of black BiOCl-Bi<sub>2</sub>O<sub>3</sub>/rGO

First, 3.0 g of BiOCl or BiOCl/GO composite was dispersed in 150 mL H<sub>2</sub>O by sonication and mechanical stirring, then reduced iron powder was added, and the mixture was under sonication and mechanical stirring for 8 h. Subsequently, 20 mL of HCl (35 wt%) was slowly added, and the mixture was maintained to be under sonication and mechanical stirring for 8 h. After Fe reduction, the excess Fe powder was fully removed from the samples by an external strong magnetic field and immersion in 0.01 mol/L HCl. Finally, the obtained product was washed by distilled water until the eluent was neutral, and dried at 80 °C for 12 h. Accordingly, the black BiOCl-Bi<sub>2</sub>O<sub>3</sub>/rGO samples were denoted as black BiOCl-Bi<sub>2</sub>O<sub>3</sub>/rGO<sub>0.02</sub>, black BiOCl-Bi<sub>2</sub>O<sub>3</sub>/rGO<sub>0.08</sub>, black BiOCl-Bi<sub>2</sub>O<sub>3</sub>/rGO<sub>0.2</sub>, black BiOCl-Bi<sub>2</sub>O<sub>3</sub>/rGO<sub>0.4</sub> and black BiOCl-Bi<sub>2</sub>O<sub>3</sub>/rGO<sub>0.6</sub> depending on the content of rGO.

### 2.4. Characterization

The crystal structure of BiOCl/GO and black BiOCl-Bi<sub>2</sub>O<sub>3</sub>/rGO was analyzed by Rigaku D/max 2200 PC X-ray diffractometer (XRD). The morphologies of BiOCl/GO and black BiOCl-Bi<sub>2</sub>O<sub>3</sub>/rGO were observed on a FEI Talos F200X scanning electron microscopy (SEM) instrument (FEI, USA) and transmission electron microscopy (TEM, JEOL, Japan). The elemental analysis was conducted by Kratox Axis Ultra DLD X-ray photoelectron spectroscopy (XPS, Daojin, Japan). UV-vis diffuse reflectance spectra (DRS) of BiOCl/GO and black BiOCl-Bi<sub>2</sub>O<sub>3</sub>/rGO were obtained using U-3900 H spectrophotometer (Hitachi, Japan). TriStar 3020 surface area and porosity analyzer (Micromeritics, USA) was used to measure the specific surface area and pore structure of samples. The photoluminescence (PL) emission spectra were obtained using HITACHI F-7000 fluorescence spectrometer (Hitachi, Japan).

### 2.5. Assessment of photocatalytic activity

Photocatalytic activities of BiOCl/GO and black BiOCl-Bi<sub>2</sub>O<sub>3</sub>/rGO were assessed by degrading 2NP under visible-light illumination. First, 0.1 g of photocatalyst was dispersed in a 10 mg/L of 2NP solution (100 mL). The suspension was kept in the dark for 30 min under continuous magnetic stirring to reach adsorption-desorption equilibrium. During visible-light irradiation, 3 mL suspension was intermittently sampled and immediately filtered using 0.45 μm membrane filter. The filtrate was analyzed using Hitachi U-3900 H UV-vis spectrophotometer, and the concentration of 2NP was calculated according to Lambert-Beer Law.

### 2.6. Active species trapping experiments

Hydroxyl radicals (·OH) and holes (h<sup>+</sup>) in the photocatalytic process of black BiOCl-Bi<sub>2</sub>O<sub>3</sub>/rGO heterojunction for 2NP degradation

were detected in presence of 1 mmol/L IPA and TEOA, respectively. To confirm the presence of superoxide radical ( $\cdot\text{O}_2^-$ ) during photocatalytic reaction, 0.1 g of photocatalyst was added into 100 mL of  $5 \times 10^{-5}$  mol/L NBT in a quartz tube, and the experiment procedure was the same as the assessment of photocatalytic activity. The concentration of NBT solution was analyzed using Hitachi U-3900 H UV-vis spectrophotometer at 259 nm according to Lambert-Beer Law.

### 2.7. The COD change of industrial wastewater in presence of BiOCl-Bi<sub>2</sub>O<sub>3</sub>/rGO<sub>0.4</sub>

The real industrial wastewater, selected from the wastewater discharge tank of Jiangxi Chemedir Biopharm-tech. Co., Ltd, was used to evaluate the practical application of black BiOCl-Bi<sub>2</sub>O<sub>3</sub>/rGO<sub>0.4</sub>. The color and initial COD value of the real industrial wastewater is dark yellow and 32,320 mg/L, respectively. The components of the wastewater were 3-methyl-2-nitrobenzoic acid (C<sub>8</sub>H<sub>7</sub>NO<sub>4</sub>), 3-methyl-2-nitrobenzoyl chloride (C<sub>8</sub>H<sub>6</sub>NO<sub>3</sub>Cl), N,3-dimethyl-2-nitrobenzamide (C<sub>9</sub>H<sub>10</sub>N<sub>2</sub>O<sub>3</sub>), 2-amino-N,3-dimethylbenzamide (C<sub>9</sub>H<sub>12</sub>N<sub>2</sub>O), 4-chloro-2-methyl-6-(methylcarbamoyl)benzenaminium chloride (C<sub>9</sub>H<sub>12</sub>N<sub>2</sub>OCl<sub>2</sub>), 2-amino-5-chloro-N,3-dimethyl benzamide (C<sub>9</sub>H<sub>11</sub>N<sub>2</sub>OCl).

The sampling procedure for COD removal of real industrial wastewater was the same as the assessment of photocatalytic activity, and COD measurement was conducted according to reference [29].

## 3. Results and discussion

### 3.1. XRD analysis

The digital photographs of pure BiOCl, BiOCl/GO and black BiOCl-Bi<sub>2</sub>O<sub>3</sub>/rGO were shown in Fig. S1 (Supporting information). Pure BiOCl is white, and the color of BiOCl/GO was gray-white before being reduced via Fe. After Fe reduction, black BiOCl-Bi<sub>2</sub>O<sub>3</sub>/rGO became deep black.

Fig. 1 shows the XRD patterns of white BiOCl, BiOCl/GO and black BiOCl-Bi<sub>2</sub>O<sub>3</sub>/rGO. It can be seen that white BiOCl and BiOCl/GO composites show characteristic peaks at 12.0°, 24.1°, 25.9°, 32.5°, 33.4°, 40.9°, 46.6°, 49.7°, 54.1°, 58.6° and 68.1°, which corresponds to (001), (002), (101), (110), (102), (200), (113), (211), (212) and (220) planes of tetragonal phase BiOCl (Fig. 1a).

After Fe reduction, there were great changes in the XRD patterns (Fig. 1b). Besides the characteristic peaks of BiOCl, the new peaks at 2θ of 28.1° and 30.5°, correspond to the (012) and (211) reflections of Bi<sub>2</sub>O<sub>3</sub>, respectively. It is interesting to note that elemental Bi metal is found in the XRD patterns due to the Fe reduction. The diffraction peaks at 2θ of 23.8°, 27.2°, 37.9°, 39.6°, 48.7° and 64.5° correspond to the

(101), (012), (104), (110), (202) and (122) reflections of metallic Bi. The above XRD analysis indicates that there is coexistence of Bi, BiOCl and Bi<sub>2</sub>O<sub>3</sub>. Significantly, there is no GO and rGO diffractions in the XRD pattern of BiOCl/GO and black BiOCl-Bi<sub>2</sub>O<sub>3</sub>/rGO heterojunction, possibly due to the high-dispersion or low content of GO or rGO.

### 3.2. XPS analysis

To further prove the reduction of GO to rGO and successful preparation of black BiOCl-Bi<sub>2</sub>O<sub>3</sub>/rGO heterojunctions, high-resolution XPS spectra of black BiOCl-Bi<sub>2</sub>O<sub>3</sub>/rGO heterojunctions were performed (Fig. 2). The Bi 4s, Bi 4p<sub>3/2</sub>, Bi 4d<sub>3/2</sub>, Bi 4d<sub>5/2</sub>, O 1s, C 1s, Cl 2p, Bi 4f<sub>5/2</sub>, Bi 5s, Bi 4f<sub>7/2</sub>, Bi 5p<sub>1/2</sub>, Bi 5p<sub>3/2</sub> and Bi 5d<sub>3/2</sub> peaks were observed in the survey scan spectra of black BiOCl-Bi<sub>2</sub>O<sub>3</sub>/rGO heterojunctions (Fig. 2a), confirming the presence of these elements in black BiOCl-Bi<sub>2</sub>O<sub>3</sub>/rGO heterojunctions. The Bi 4f spectra can be deconvoluted into five (Fig. 2b). The binding energy peaks of Bi 4f<sub>7/2</sub> and Bi 4f<sub>5/2</sub> for BiOCl located at 159.6 and 164.9 eV with a peak splitting of 5.3 eV [30]. The peaks with binding energy of 160.5 and 165.8 eV were assigned to Bi 4f<sub>7/2</sub> and Bi 4f<sub>5/2</sub> of Bi<sub>2</sub>O<sub>3</sub>, respectively. The peaks at 157.9 eV were assigned to metallic Bi [31]. Two binding energy peaks at 198.5 and 200.1 eV were assigned to the Cl 2p<sub>3/2</sub> and Cl 2p<sub>1/2</sub> region for BiOCl, respectively (Fig. 2c). The O 1s core level spectrum (Fig. 2d) exhibited three different peaks at 530.7, 531.8 and 532.5 eV, which were related to O<sup>2-</sup> anions in BiOCl, C=O and C=O, respectively. The deconvoluted XPS peaks of C 1s (Fig. 2e) centered at the binding energies of 284.8, 285.9, 287.3 and 289.3 eV were assigned to C—C, C=C, C—OH and O=C=O, respectively.

### 3.3. Raman analysis

In order to confirm the formation of Bi<sub>2</sub>O<sub>3</sub>, Bi and rGO by Fe reduction, the Raman spectra of white BiOCl and black BiOCl-Bi<sub>2</sub>O<sub>3</sub>/rGO were analyzed (Fig. 3). In the Raman spectrum of white BiOCl, four distinguishable bands were observed at 63, 143, 200 and 396 cm<sup>-1</sup>. The Raman peaks at 63, 143 and 200 cm<sup>-1</sup> correspond to the A<sub>1g</sub> external Bi—Cl stretching mode, A<sub>1g</sub> internal Bi—Cl stretching mode and E<sub>g</sub> internal of Bi—Cl stretching mode in BiOCl, respectively. The relatively weak peak at 396 cm<sup>-1</sup> can be assigned to the E<sub>g</sub> and B<sub>1g</sub> bands produced by motion of the oxygen atoms. For black BiOCl-Bi<sub>2</sub>O<sub>3</sub>/rGO<sub>0.4</sub>, the band centered at 95 cm<sup>-1</sup> can be attributed to the first-order scattering A<sub>1g</sub> modes of Bi, the band centered at 131 cm<sup>-1</sup> corresponds to the A<sub>1g</sub> internal Bi—Cl stretching mode, the band centered at 305 cm<sup>-1</sup> corresponds to the Bi—O stretching, and the peaks at 1325 and 1597 cm<sup>-1</sup> can be assigned to the D bands of rGO.

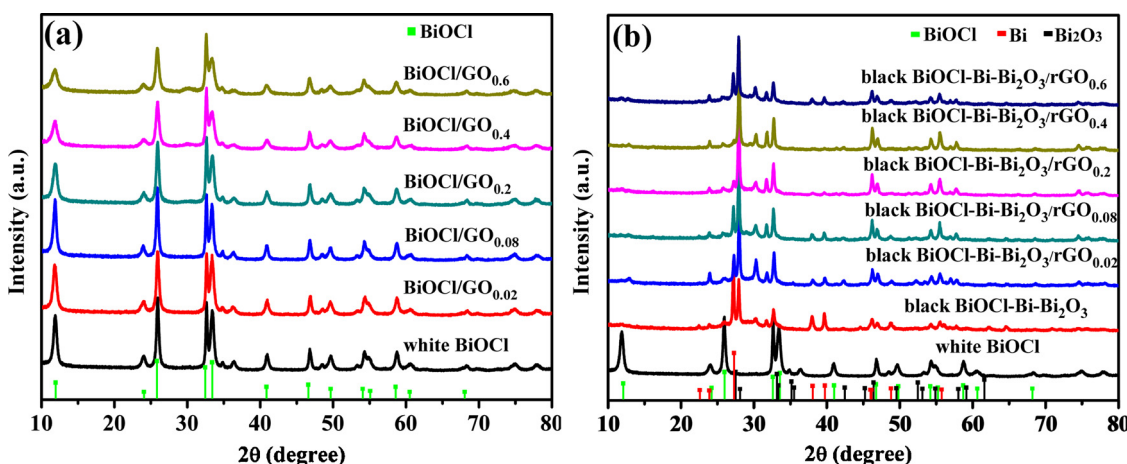


Fig. 1. XRD patterns of white BiOCl, BiOCl/GO and black BiOCl-Bi<sub>2</sub>O<sub>3</sub>/rGO nanosheet heterojunctions.

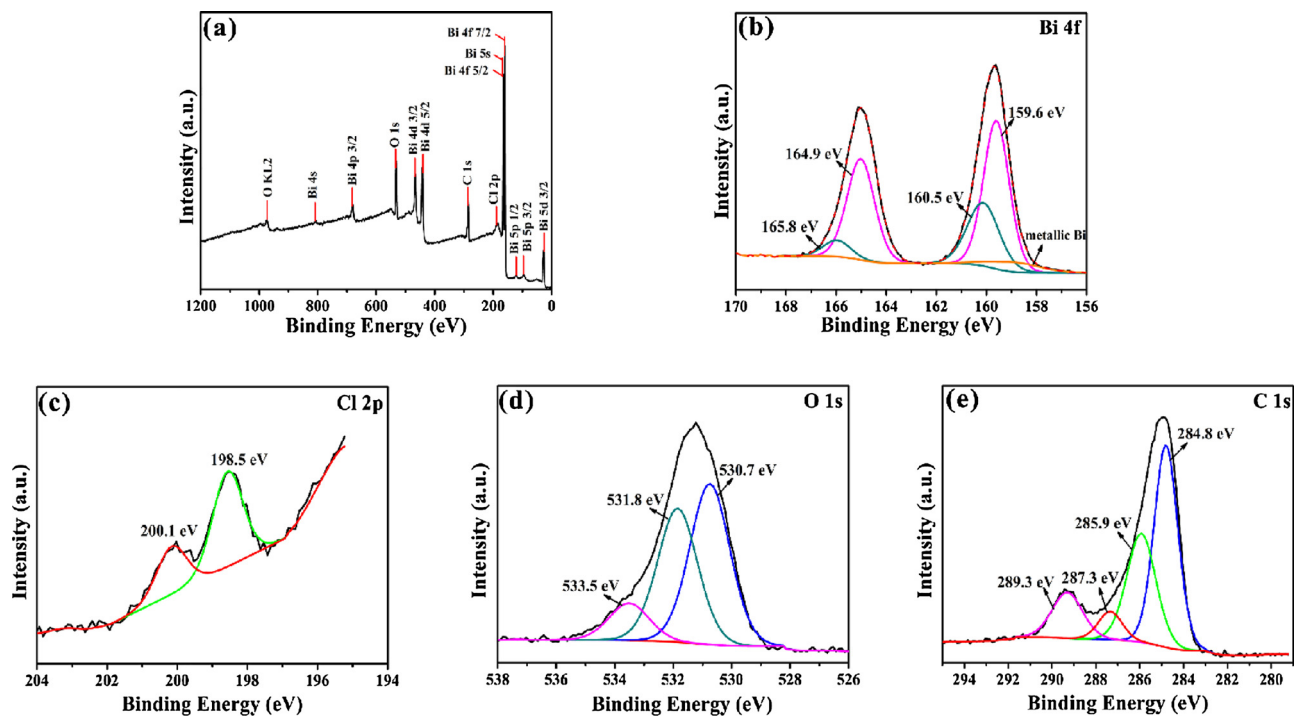


Fig. 2. XPS spectra of black BiOCl-Bi-Bi<sub>2</sub>O<sub>3</sub>/rGO<sub>0.4</sub> in (a) the survey spectrum, (b) Bi 4f, (c) Cl 2p, (d) O 1s and (e) C 1s binding energy regions.

### 3.4. SEM analysis

Fig. 4 shows the SEM images of BiOCl/GO and black BiOCl-Bi<sub>2</sub>O<sub>3</sub>/rGO heterojunctions. The interface surface of BiOCl/GO presented obvious compact sandwich structure with thickness of 200–400 nm, consisting of several 2D nanosheets with thickness of 20–40 nm. After Fe reduction, there is a great change in the morphology, and a large quantity of irregular sheets are observed. The thickness of black BiOCl-Bi-Bi<sub>2</sub>O<sub>3</sub>/rGO irregular nanosheets become much smaller, and the nanosheets randomly intersect with each other.

### 3.5. TEM and HRTEM analysis

TEM and HRTEM measurements were performed to further characterize the morphology of black BiOCl-Bi-Bi<sub>2</sub>O<sub>3</sub>/rGO heterojunctions (Fig. 5). As can be seen from Fig. 5a and b, the sheet-shaped nanomaterials were covered with rGO sheets. In addition, as shown in Fig. 5c and d, two sets of lattice fringes with a lattice spacing of 0.342 and 0.275 nm correspond to the BiOCl (101) and (110) plane, respectively. The interplanar spacings of 0.227 and 0.318 nm match the spacing

distance of metallic Bi (110) and Bi<sub>2</sub>O<sub>3</sub> (012) plane, respectively. The TEM and HRTEM analysis further confirmed the formation of metallic Bi and Bi<sub>2</sub>O<sub>3</sub>.

### 3.6. Specific surface areas and porous structures

The nitrogen adsorption-desorption isotherm and the pore size distribution curves of BiOCl/GO and black BiOCl-Bi-Bi<sub>2</sub>O<sub>3</sub>/rGO with different rGO content were shown in Fig. S2 and Fig. S3. According to the Brunauer-Deming-Deming-Teller (BDDT) classification, the isotherms of white BiOCl and BiOCl/GO belong to type IV, implying the presence of mesopores (2–50 nm). The shape of the hysteresis loop is of type H3, which is related with the accumulation of nanoplates, giving rise to slit-like pores (Fig. S2). Moreover, the BET surface areas of BiOCl/GO are dependent on the GO content. The BET surface areas of BiOCl/GO increase with increasing the GO content from 0 to 0.4, while further increasing GO content leads to the decrease of the BET surface areas of BiOCl/GO. After the Fe reduction of BiOCl/GO to black BiOCl-Bi-Bi<sub>2</sub>O<sub>3</sub>/rGO, there is no change in the type and hysteresis loop of the isotherms, but the BET surface areas decrease (Fig. S3 and Table S1).

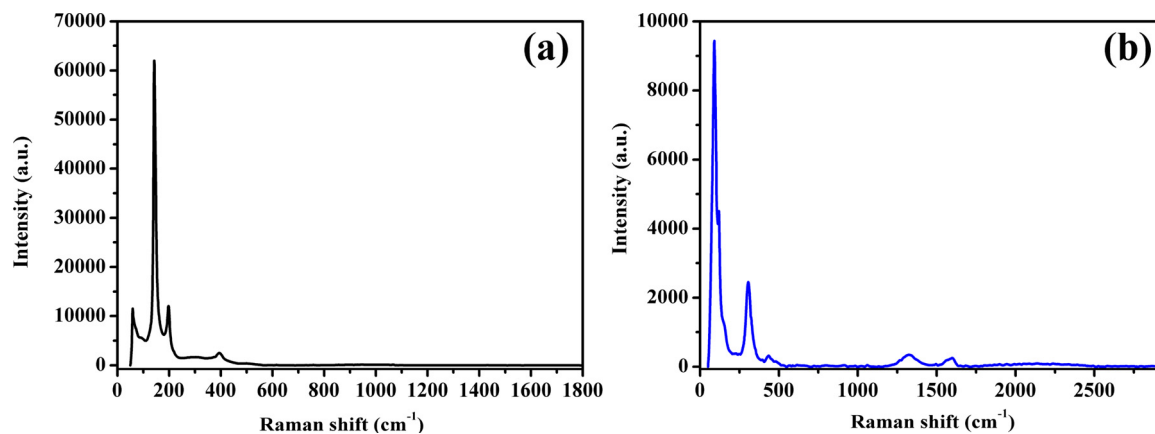


Fig. 3. Raman spectra of (a) white BiOCl and (b) black BiOCl-Bi-Bi<sub>2</sub>O<sub>3</sub>/rGO<sub>0.4</sub>.

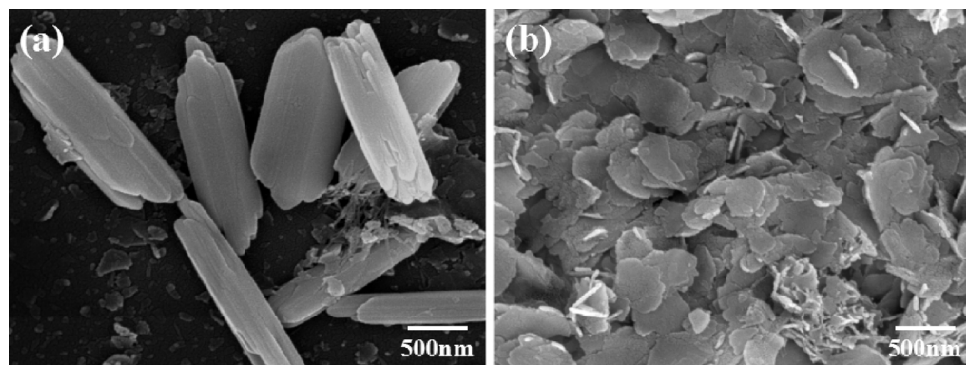


Fig. 4. SEM images of (a) BiOCl/GO<sub>0.4</sub> and (b) black BiOCl-Bi<sub>2</sub>O<sub>3</sub>/rGO<sub>0.4</sub>.

The decrease of BET surface areas indicates that the reduction of Fe brings about the change in the surface and structure of materials.

### 3.7. UV-vis diffuse reflectance spectra

The UV-vis diffuse reflectance spectra of pure BiOCl, BiOCl/GO and black BiOCl-Bi<sub>2</sub>O<sub>3</sub>/rGO were shown in Fig. S4. Before Fe reduction, the light absorption intensity of BiOCl/GO is associated with GO content. Pure BiOCl has a weak visible-light absorption. With increasing GO content from 0 to 0.02, the visible-light absorption intensity of BiOCl/GO is boosted up, and the absorption edges of BiOCl/GO composites shift to longer wavelength, while further increasing the GO content leads to a slight decrease in visible-light absorption. These results indicate that proper GO content can enhance the visible-light absorption. After Fe reduction, the visible-light absorption is significantly enhanced.

The band positions of white BiOCl and BiOCl/GO composites can be determined according to the following equation:

$$(\alpha h\nu)^2 = A(h\nu - E_g)^n$$

where  $\alpha$  is the absorption coefficient,  $h$  is Planck's constant,  $\nu$  is light frequency,  $A$  is a constant and  $E_g$  is the band gap energy,  $n = 1$  for direct-band-gap semiconductor and  $n = 4$  for indirect-band-gap

semiconductor. The plot of  $(\alpha h\nu)^{1/2}$  versus  $h\nu$  is shown in Fig. S4b, and  $E_g$  values were obtained by prolonging the tangent of the plots to  $(\alpha h\nu)^{1/2} = 0$ . The  $E_g$  values of pure BiOCl, BiOCl/GO<sub>0.02</sub>, BiOCl/GO<sub>0.08</sub>, BiOCl/GO<sub>0.2</sub>, BiOCl/GO<sub>0.4</sub> and BiOCl/GO<sub>0.6</sub> are 3.60, 3.55, 3.47, 3.25, 3.15 and 3.20 eV, respectively.

### 3.8. PL emission spectra

Solid fluorescence spectroscopy has been widely adopted to investigate the charge separation and transfer efficiency of semiconductors. Fig. S5 shows PL emission spectra of white BiOCl, BiOCl/GO and black BiOCl-Bi<sub>2</sub>O<sub>3</sub>/rGO heterojunctions. The PL intensity of BiOCl/GO before Fe reduction is more intense than that of black BiOCl-Bi<sub>2</sub>O<sub>3</sub>/rGO heterojunctions. The PL intensity of BiOCl/GO is associated with the GO content. Increasing GO content from 0 to 0.4 decreases the PL intensity of BiOCl/GO composites, but further increasing GO content from 0.4 to 0.6 leads to the enhancement of PL signals. The PL intensity trend of black BiOCl-Bi<sub>2</sub>O<sub>3</sub>/rGO is similar to that of BiOCl/GO. The PL results indicated that the formation of black BiOCl-Bi<sub>2</sub>O<sub>3</sub>/rGO heterojunctions by Fe reduction retarded the recombination of photogenerated electron-hole pairs more effectively, and proper rGO can promote the separation and transfer of photo-generated electron-hole pairs.

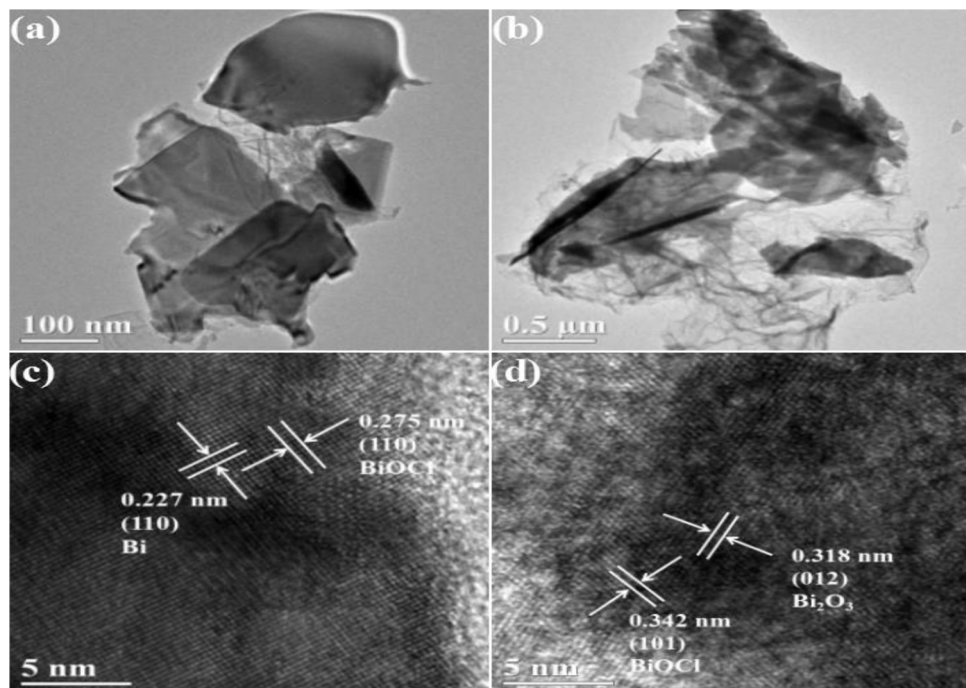


Fig. 5. TEM (a, b) and HRTEM (c, d) images of black BiOCl-Bi<sub>2</sub>O<sub>3</sub>/rGO<sub>0.4</sub>.

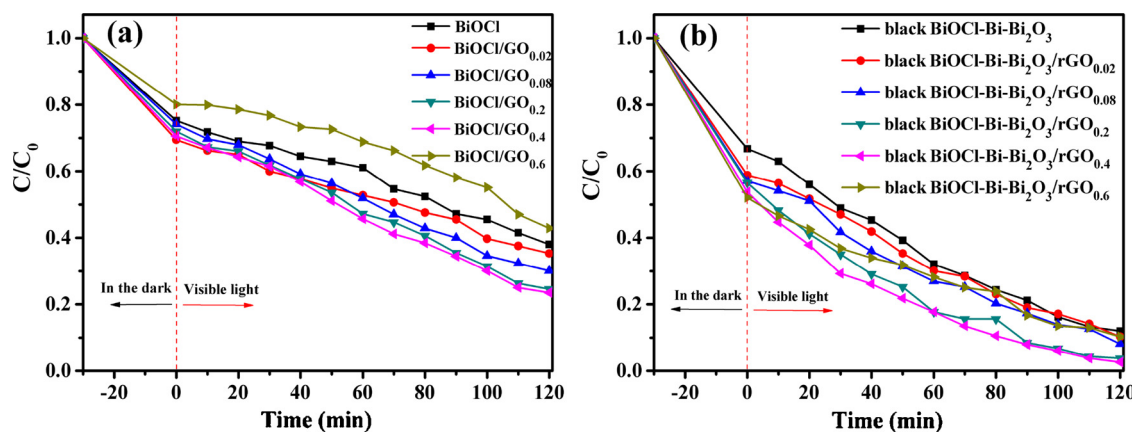


Fig. 6. Photocatalytic activities of BiOCl/GO and black BiOCl-Bi-Bi<sub>2</sub>O<sub>3</sub>/rGO in degrading 2NP.

PL emission was also used as a useful technique to examine the oxygen vacancy. In the PL emission spectra of white BiOCl, BiOCl/GO and black BiOCl-Bi-Bi<sub>2</sub>O<sub>3</sub>/rGO, there are two PL emission peaks centered at 451.5 and 469.4 nm. The PL emission peak at 469.4 nm indicates the presence of oxygen vacancies. The oxygen vacancies, as the trapping centers of photogenerated electrons, makes it difficult for the photogenerated electrons to be combined with the holes in the BiOCl conduction band, which enhances the separation efficiency of photo-generated carriers.

### 3.9. Photocatalytic activity

#### 3.9.1. The evaluation of photocatalytic activity for degradation of 2NP

The visible-light photocatalytic activities of white BiOCl, BiOCl/GO, and black BiOCl-Bi-Bi<sub>2</sub>O<sub>3</sub>/rGO heterojunction were evaluated by degrading aqueous 2NP solution. Fig. 6a shows the photocatalytic degradation curves of 2NP over BiOCl/GO before Fe reduction. With the increase of GO content from 0 to 0.4, the photocatalytic activities of BiOCl/GO were enhanced, but decreased with further increasing GO content. The order of photocatalytic activities were BiOCl/GO<sub>0.4</sub> > BiOCl/GO<sub>0.2</sub> > BiOCl/GO<sub>0.08</sub> > BiOCl/GO<sub>0.02</sub> > BiOCl > BiOCl/GO<sub>0.6</sub>. BiOCl/GO<sub>0.4</sub> exhibited the highest photocatalytic activity with 76.5% degradation efficiency of 2NP. After Fe reduction, the photocatalytic activities were significantly improved (Fig. 6b), and the order of photocatalytic activities change slightly. The photocatalytic activities of black BiOCl-Bi-Bi<sub>2</sub>O<sub>3</sub>/rGO heterojunction increased from 88% to 99.7% with increasing the rGO content from 0 to 0.4, and black BiOCl-Bi-Bi<sub>2</sub>O<sub>3</sub>/rGO<sub>0.4</sub> exhibits the highest photocatalytic activities with almost complete degradation of 2NP due to the beneficial role of the optimum amount of rGO to the charge generation and transfer at heterojunction interfaces, which is higher than the reported degradation efficiency of 2NP by V<sub>2</sub>O<sub>5</sub>-ZnO composites (96%) [32]. The photocatalytic activity decreased with further increasing rGO content. The order of photocatalytic activities was as follows: black BiOCl-Bi-Bi<sub>2</sub>O<sub>3</sub>/rGO<sub>0.4</sub> > black BiOCl-Bi-Bi<sub>2</sub>O<sub>3</sub>/rGO<sub>0.2</sub> > black BiOCl-Bi-Bi<sub>2</sub>O<sub>3</sub>/rGO<sub>0.08</sub> > black BiOCl-Bi-Bi<sub>2</sub>O<sub>3</sub>/rGO<sub>0.02</sub> = black BiOCl-Bi-Bi<sub>2</sub>O<sub>3</sub>/rGO<sub>0.6</sub> > black BiOCl-Bi-Bi<sub>2</sub>O<sub>3</sub> > black BiOCl.

To further explore the photocatalytic degradation pathway of 2NP, 2NP and its degradation intermediates were studied by using HPLC-MS. The mass peaks and corresponding intermediates were shown in Fig. 7. On the basis of the *m/z* values of intermediates, we have inferred the degradation pathway of 2NP in presence of black BiOCl-Bi-Bi<sub>2</sub>O<sub>3</sub>/rGO under visible-light illumination (Fig. 8). 2NP underwent ring opening to form small molecules. Finally, small molecules can be

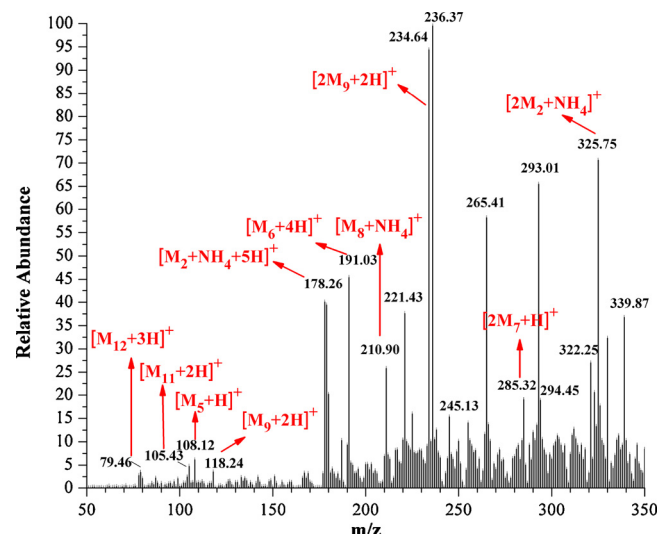


Fig. 7. Mass spectra of 2NP and its intermediates during the photodegradation process.

further mineralized into NO<sub>3</sub><sup>-</sup>, CO<sub>2</sub> and H<sub>2</sub>O through a series of oxidation reaction.

#### 3.9.2. The application in the treatment of real industrial wastewater

Chemical oxygen demand (COD) is an important indicator of organic pollution in water bodies. Thus, the practical application of black BiOCl-Bi-Bi<sub>2</sub>O<sub>3</sub>/rGO was evaluated by monitoring the COD removal of real industrial wastewater (Fig. 9). The original COD of real industrial wastewater was 32,320 mg/L. The COD of industrial wastewater decreased to 10,530 mg/L (67.4% COD removal efficiency) in presence of BiOCl-Bi-Bi<sub>2</sub>O<sub>3</sub>/rGO under visible-light irradiation for 11 h. When both BiOCl-Bi-Bi<sub>2</sub>O<sub>3</sub>/rGO and 1 mL 30% H<sub>2</sub>O<sub>2</sub> were added in industrial wastewater, the COD removal efficiency reached 70.3%.

### 3.10. Photocatalytic mechanism

To examine the reactive oxidative species during the photocatalytic degradation of 2NP and elucidate the photocatalytic mechanism of black BiOCl-Bi-Bi<sub>2</sub>O<sub>3</sub>/rGO, a colorless molecular probe NBT was adopted to quantify superoxide anion radicals (·O<sub>2</sub><sup>-</sup>), TEOA was used

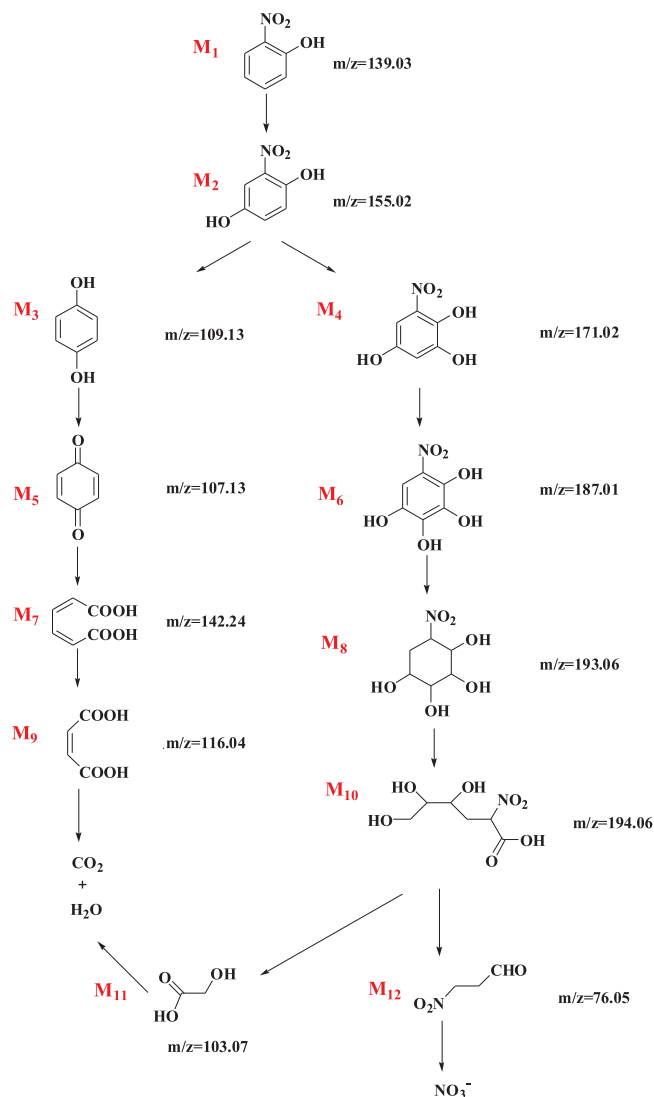


**Fig. 8.** The degradation pathway of 2NP in black BiOCl-Bi<sub>2</sub>O<sub>3</sub>/rGO suspension under visible-light irradiation.

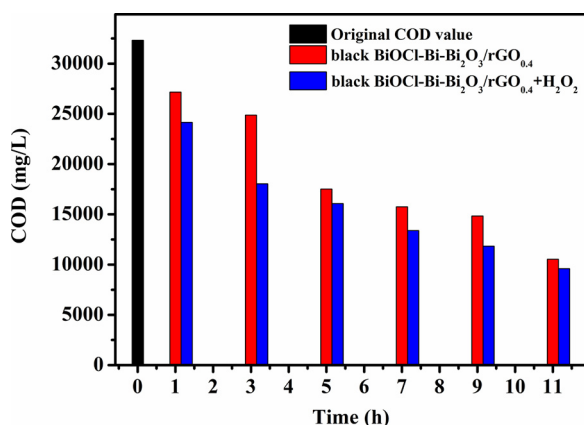


**Fig. 9.** The COD change of real industrial wastewater in presence of black BiOCl-Bi<sub>2</sub>O<sub>3</sub>/rGO<sub>0.4</sub> under visible-light irradiation.

as hole ( $h^+$ ) quencher, and IPA was chosen as  $\cdot OH$  quencher. In the black BiOCl-Bi<sub>2</sub>O<sub>3</sub>/rGO<sub>0.4</sub> photocatalytic system, the degradation efficiency of 2NP over black BiOCl-Bi<sub>2</sub>O<sub>3</sub>/rGO<sub>0.4</sub> was 99.7% in

absence of scavengers, and the degradation efficiency of 2NP reduced to 71.6% and 5.6% in case of adding TEOA and IPA into the photocatalytic system, respectively (Fig. 10a). Notably, 62.6% NBT degradation efficiency can be achieved by black BiOCl-Bi<sub>2</sub>O<sub>3</sub>/rGO<sub>0.4</sub> (Fig. 10b). These above trapping experiments suggested  $\cdot OH$ ,  $\cdot O_2^-$  and  $h^+$  play joint roles in photocatalytic degradation of 2NP.

According to the above experimental results, a possible photocatalytic mechanism of Z-scheme black BiOCl-Bi<sub>2</sub>O<sub>3</sub>/rGO heterojunctions including multiple charge transfer channels and oxygen vacancy was proposed (Fig. 11). Under visible-light irradiation, the electrons in the VB of Bi<sub>2</sub>O<sub>3</sub> can be excited to its CB, while the electrons in the VB of BiOCl can only be excited up to its oxygen vacancies. Simultaneously, equal amounts of holes are generated in their VB. The photogenerated electrons in the CB of Bi<sub>2</sub>O<sub>3</sub> can be transferred to the VB of BiOCl via Bi-bridge and rGO. The photogenerated electrons in oxygen vacancies of BiOCl can capture and reduce the dissolved oxygen for formation of superoxide radical ( $\cdot O_2^-$ ). Meanwhile,  $\cdot OH$  can be produced from  $h^+$  in the VB of Bi<sub>2</sub>O<sub>3</sub> since the VB of Bi<sub>2</sub>O<sub>3</sub> are more positive than  $OH^-/\cdot OH$  (1.99 V). The  $\cdot O_2^-$ ,  $\cdot OH$  and the photo-generated holes left in the VB of Bi<sub>2</sub>O<sub>3</sub> can then participate in 2NP degradation.

### 3.11. Reusability of black BiOCl-Bi<sub>2</sub>O<sub>3</sub>/rGO<sub>0.4</sub>

The reusable performance of catalysts is crucial to the practical application, since it make significant contribution to lowering the operational cost. In order to test the reusability of black BiOCl-Bi<sub>2</sub>O<sub>3</sub>/rGO<sub>0.4</sub>, the reusability performance of black BiOCl-Bi<sub>2</sub>O<sub>3</sub>/rGO<sub>0.4</sub> heterojunction was verified by recycling and reusing black BiOCl-Bi<sub>2</sub>O<sub>3</sub>/rGO<sub>0.4</sub> sample under the same conditions as the original sample, and the results are shown in Fig. 12. The photocatalytic activities remain practically at the same level after four degradation-regeneration cycles, implying that black BiOCl-Bi<sub>2</sub>O<sub>3</sub>/rGO<sub>0.4</sub> heterojunction shows excellent recyclability, and can be used repeatedly, thereby reducing the cost.

The high stability of BiOCl-Bi<sub>2</sub>O<sub>3</sub>/rGO was further confirmed by XRD and XPS. Compared with the XRD pattern of fresh BiOCl-Bi<sub>2</sub>O<sub>3</sub>/rGO, the position and characteristic diffraction peaks of the recovered BiOCl-Bi<sub>2</sub>O<sub>3</sub>/rGO do not change obviously (Supporting Information, Fig. S6), indicating the stable crystal structure of BiOCl-Bi<sub>2</sub>O<sub>3</sub>/rGO during the photocatalytic process. The surface composition and chemical state of the fresh and recovered BiOCl-Bi<sub>2</sub>O<sub>3</sub>/rGO was also investigated (Supporting Information, Fig. S7). There is no change in the surface composition and peak positions of Cl 2p, O 1s and C 1s, but binding energies of Bi 4f shift slightly (about 0.2 eV), further confirming the stable surface composition BiOCl-Bi<sub>2</sub>O<sub>3</sub>/rGO and chemical environment of Cl 2p, O 1s and C 1s.

## 4. Conclusions

We successfully fabricated a novel graphene-functionalized Bi-bridge Z-scheme black BiOCl/Bi<sub>2</sub>O<sub>3</sub> heterojunction catalysts with oxygen vacancies using *in situ* Fe reduction of BiOCl/GO nanoplates. Compared with BiOCl/GO, the black BiOCl-Bi<sub>2</sub>O<sub>3</sub>/rGO heterojunctions show enhanced visible-light absorption, and exhibit much higher visible-light photocatalytic activity in degrading 2NP. The photocatalytic activity of BiOCl-Bi<sub>2</sub>O<sub>3</sub>/rGO heterojunctions relies heavily on rGO content, and the optimal BiOCl-Bi<sub>2</sub>O<sub>3</sub>/rGO<sub>0.4</sub> exhibited the highest photocatalytic activity with 99.7% degradation efficiency of 2NP, which is attributed to the synergistic effect of proper bandgap matching between black BiOCl and Bi<sub>2</sub>O<sub>3</sub>, multiple charge transfer channels including Bi-bridge and rGO, and efficient charge separation. More importantly, BiOCl-Bi<sub>2</sub>O<sub>3</sub>/rGO heterojunction can effectively treat real industrial wastewater with 70.3% COD removal efficiency, and it shows superior stability with no decrease of photocatalytic

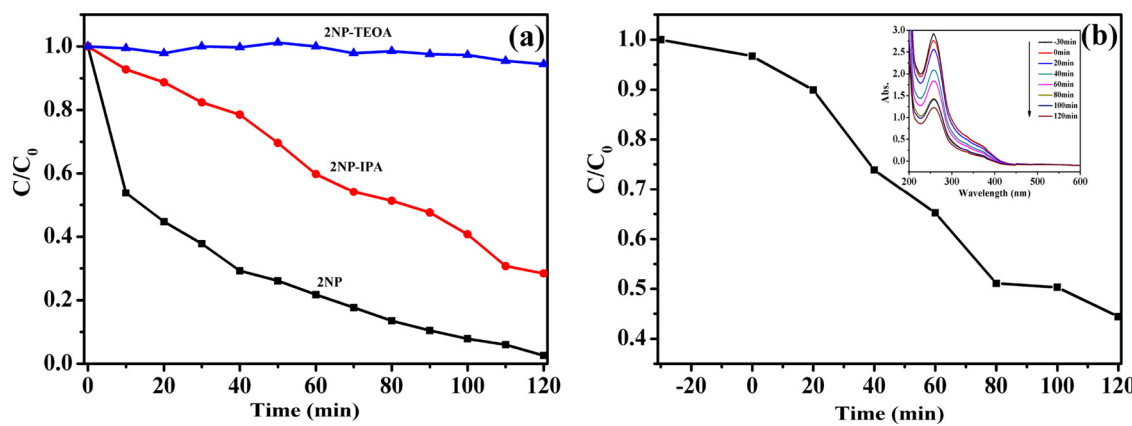


**Fig. 10.** (a) Photocatalytic degradation efficiencies of 2NP on black BiOCl-Bi-Bi<sub>2</sub>O<sub>3</sub>/rGO in the presence of different scavengers under visible-light irradiation; (b) Photocatalytic degradation of NBT under visible-light irradiation (inset: UV-vis absorption spectra of NBT during photocatalytic degradation).

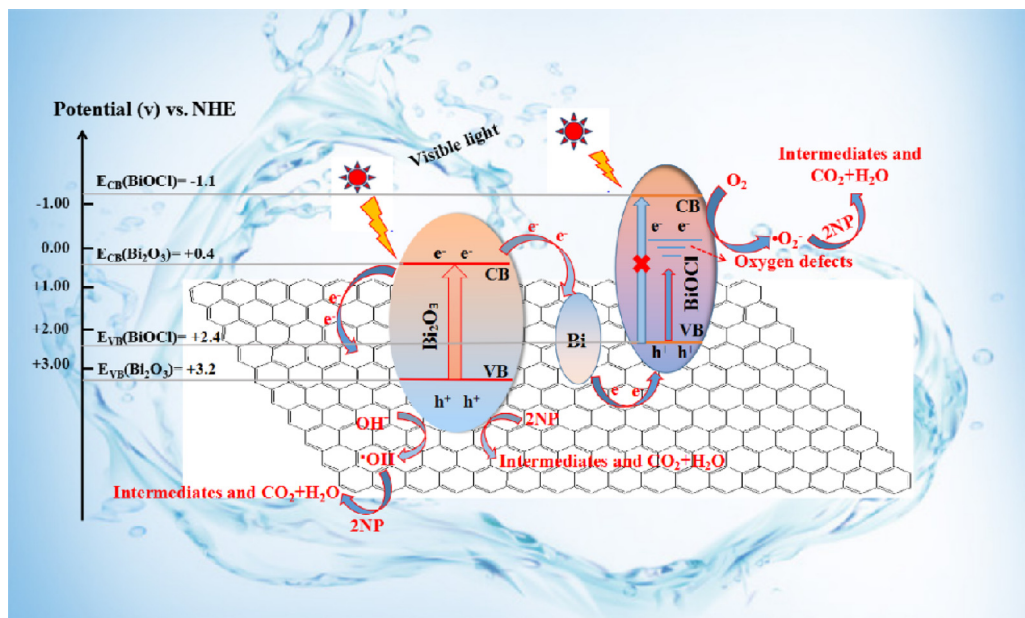


**Fig. 11.** Possible photocatalytic mechanism of Z-scheme black BiOCl-Bi-Bi<sub>2</sub>O<sub>3</sub>/rGO heterojunctions including multiple charge transfer channels and oxygen vacancy.

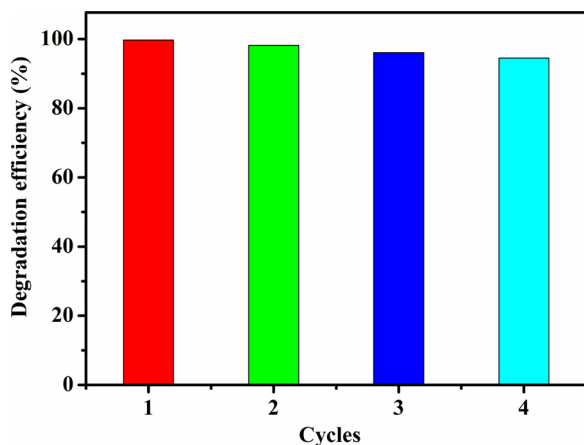


**Fig. 12.** The reusability of Z-scheme black BiOCl-Bi-Bi<sub>2</sub>O<sub>3</sub>/rGO heterojunctions.

activity and stable crystal structure in four repeated runs. Additionally, a distinctive photocatalytic mechanism of Z-scheme black BiOCl-Bi-Bi<sub>2</sub>O<sub>3</sub>/rGO heterojunctions including multiple charge transfer channels

and oxygen vacancies was proposed.

#### Acknowledgments

This work was supported by National Natural Science Foundation of China (51741806, 51720105001, 51238002), Department of Education Fund of Jiangxi Province (GJJ150742), Natural Science Foundation of Jiangxi Province (2016BAB206117), Science Fund for Excellent Young Scholars of Jiangxi Province (20162BCB23038). D. D. Dionysiou also acknowledges support from the University of Cincinnati through a UNESCO co-Chair Professor position on “Water Access and Sustainability” and the Herman Schneider Professorship in the College of Engineering and Applied Sciences.

#### Appendix A. Supplementary data

Supplementary material related to this article can be found, in the online version, at doi:<https://doi.org/10.1016/j.apcatb.2018.05.004>.

#### References

- [1] S. Miralles-Cuevas, I. Oller, A. Agüera, M. Llorca, J.A. Sánchez Pérez, S. Malato, J.

- Hazard. Mater. 323 (2017) 442–451.
- [2] X. Zhang, C. Chen, P. Lin, A. Hou, Z. Niu, J. Wang, Environ. Sci. Technol. 45 (2011) 161–167.
- [3] R.P. Schwarzenbach, T. Egli, T.B. Hofstetter, U.V. Gunten, B. Wehrli, Environ. Resour. 35 (2010) 109–136.
- [4] W. Wu, C. Jiang, V.A. Roy, Nanoscale 7 (2014) 38–58.
- [5] H. Cheng, B. Huang, Y. Dai, Nanoscale 6 (2014) 2009–2026.
- [6] Y. Wang, Q. Wang, X. Zhan, F. Wang, M. Safdar, J. He, Nanoscale 5 (2013) 8326–8339.
- [7] G. Darabdhara, P.K. Boruah, P. Borthakur, N. Hussain, M.R. Das, T. Ahamad, S.M. Alshehri, V. Malgras, K.C. Wu, Y. Yamauchi, Nanoscale 8 (2016) 8276–8287.
- [8] E.K. Sackmann, A.L. Fulton, D.J. Beebe, Nature 507 (2014) 181–189.
- [9] S. Liu, C. Liu, W. Wang, B. Cheng, J. Yu, Nanoscale 4 (2012) 3193–3200.
- [10] Y. Gao, P. Fang, Z. Liu, F. Chen, Y. Liu, D. Wang, Y. Dai, Chem. Asian J. 8 (2013) 204–211.
- [11] T. Hisatomi, J. Kubotaa, K. Domen, Chem. Soc. Rev. 43 (2014) 7520–7535.
- [12] M.L. Guan, C. Xiao, J. Zhang, S.J. Fan, Q. Chen, J.F. Xie, J. Am. Chem. Soc. 135 (2013) 10411–10417.
- [13] B. Sarwan, B. Pare, A.D. Acharya, S.B. Jonnalagadda, J. Photochem. Photobiol. B: Biol. 116 (2012) 48–55.
- [14] K.L. Zhang, C.M. Liu, F.Q. Huang, C. Zheng, W.D. Wang, Appl. Catal. B: Environ. 68 (2006) 125–129.
- [15] X. Chen, L. Liu, P.Y. Yu, S.S. Mao, Science 331 (2011) 746–750.
- [16] T. Ihara, M. Miyoshi, Y. Iriyama, O. Matsumoto, S. Sugihara, Appl. Catal. B: Environ. 42 (2003) 403–409.
- [17] L.Q. Ye, K.J. Deng, F. Xu, L.H. Tian, T.Y. Peng, L. Zan, Phys. Chem. Chem. Phys. 14 (2012) 82–85.
- [18] S.Y. Chai, M.H. Jung, Y.J. Kim, A.K. Chakraborty, D.W. Jung, J. Catal. 262 (2009) 144–149.
- [19] J. Jiang, K. Zhao, X. Xiao, L.Z. Zhang, J. Am. Chem. Soc. 134 (2012) 4473–4476.
- [20] X. Zhang, Z. Ai, F. Jia, L.Z. Zhang, J. Phys. Chem. C. 112 (2008) 747–753.
- [21] L. Zhang, W. Wang, J. Yang, Z. Chen, W. Zhang, L. Zhou, S. Liu, Appl. Catal. A: Gen. 308 (2006) 105–110.
- [22] S.Y. Wang, X.L. Yang, X.H. Zhang, X. Ding, Z. Yang, K. Dai, H. Chen, Appl. Surf. Sci. 391 (2017) 194–201.
- [23] J. Jin, J. Yu, D. Guo, C. Cui, W. Ho, Small 11 (2015) 5262–5271.
- [24] Y. Bai, P.Q. Wang, J.Y. Liu, X.J. Liu, RSC Adv. 4 (2014) 19456–19461.
- [25] K. Maeda, ACS Catal. 3 (2013) 1486–1503.
- [26] H.L. Wang, L.S. Zhang, Z.G. Chen, J.Q. Hu, S.J. Li, Z.H. Wang, J.S. Liu, X.C. Wang, Chem. Soc. Rev. 43 (2014) 5234–5244.
- [27] L. Ye, J. Liu, C. Gong, L. Tian, T. Peng, L. Zan, ACS Catal. 2 (2012) 1677–1683.
- [28] H. Alves, A.S. Molinari, H.X. Xie, A.F. Morpurgo, Nat. Mater. 7 (2008) 574–580.
- [29] F. Deng, L. Zhao, X. Luo, S. Luo, D.D. Dionysiou, Chem. Eng. J. 333 (2018) 423–433.
- [30] C.H. Wang, C.L. Shao, Y.C. Liu, L.N. Zhang, Scripta Mater. 59 (2008) 332–335.
- [31] Y. Yu, C.Y. Cao, H. Liu, P. Li, F.F. Wei, Y. Jiang, W.G. Song, J. Mater. Chem. 2 (2014) 1677–1681.
- [32] M. Aslam, I.M.I. Ismail, T. Almeelbi, N. Salah, S. Chandrasekaran, A. Hameed, Chemosphere. 117 (2014) 115–123.